

Creep failure of honeycombs made by rapid prototyping

P. E. Seiler^a, H. C. Tankasala^a, N. A. Fleck^{a,*}

^aDepartment of Engineering, University of Cambridge, Cambridge CB2 1PZ, United Kingdom

Abstract

Additive manufacture and rapid prototyping are versatile methods for the generation of lattice materials for applications in the creep regime. However, these techniques introduce defects that can degrade the macroscopic creep strength. In the present study, the uniaxial tensile response of two-dimensional PMMA lattices is measured in the visco-plastic regime: tests are performed at 100 °C which is slightly below the glass transition temperature T_g of PMMA. Both *as-manufactured* defects (Plateau borders and strut thickness variation) and *as-designed* defects (missing cell walls, solid inclusions, and randomly perturbed joints) are introduced. The dispersion in macroscopic strength is measured for relative densities in the range of 0.07 to 0.19. It is observed that initial failure of the lattice is diffuse in nature: struts fail at a number of uncorrelated locations, followed by the development of a single macroscopic crack transverse to the loading direction. In contrast, the same PMMA lattice fails in a correlated, brittle manner at room temperature. An FE study is performed to gain insight into the diffuse failure mode and the role played by *as-manufactured* defects, including the dispersion in tensile strength of individual struts of the lattice. A high damage tolerance to *as-designed* defects is observed experimentally: there is negligible knock-down in strength due to the removal of cell walls or to the presence of solid inclusions. These findings aid the design and manufacture of damage tolerant lattices in the creep regime.

Keywords: lattice materials, visco-plastic, tensile strength, rapid prototyping

*Corresponding author

Email addresses: pes34@cam.ac.uk (P. E. Seiler), hct30@cam.ac.uk (H. C. Tankasala), naf1@eng.cam.ac.uk (N. A. Fleck)

1. Introduction

Foams and lattices are increasingly used in engineering applications due to advances in additive manufacturing methods. A recent example is the use of micro-architected polymeric soles of running shoes. There is a need to develop tough, stiff, and lightweight lattices, with high creep resistance for high temperature applications, e. g. heat exchangers, thermal insulation and catalytic converters [1]. Whilst the creep behaviour of foams has been reported [2–11], few studies detail the tensile response of rate-sensitive, visco-plastic lattices [3, 12]. The present study addresses this gap in the literature, especially in regard to as-manufactured and as-designed imperfections and the implication of these two classes of imperfection on the macroscopic response. The present study is companion to that of the recent paper [13] on the brittle response of polymethyl methacrylate (PMMA) lattices tested at room temperature. In particular, the defect-sensitivity of creep strength is compared with that of brittle strength as taken from [13], for the same geometries and same manufacturing technique.

1.1. Hexagonal lattices

A regular two-dimensional (2D) hexagonal lattice is shown in Fig. 1(b). It comprises struts of length ℓ and in-plane thickness t such that, for $t/\ell < 0.2$, the relative density $\bar{\rho}$ of the lattice is given by

$$\bar{\rho} = \frac{2}{\sqrt{3}} \frac{t}{\ell} \quad (1)$$

as derived in Ref. [1]. Under macroscopic uniaxial loading, the hexagonal lattice is bending-dominated [1]. Consequently, the macroscopic stiffness E and the macroscopic strength σ_f^∞ of a brittle hexagonal lattice scale with relative density $\bar{\rho}$ according to

$$E = \frac{3}{2} \bar{\rho}^3 E_s \quad \text{and} \quad \sigma_f^\infty = \frac{1}{3} \bar{\rho}^2 \sigma_{fs} \quad (2)$$

in terms of the Young's modulus E_s and tensile strength σ_{fs} of the parent solid. In the present study, we select polymethyl methacrylate (PMMA) as the cell wall material of the hexagonal lattice since it behaves in an elastic-brittle manner at room temperature, but is visco-plastic at temperatures close to the glass transition

temperature, T_g .

The presence of as-manufactured defects significantly degrade the macroscopic tensile strength of elastic-brittle hexagonal lattices [13]. For example, a dispersion in strut thickness and in tensile strength of individual struts within the lattice knocks down the macroscopic strength. Successive strut failure occurs in the vicinity of a previously failed strut, and this leads to a correlated failure mode. Ultimately, a single macroscopic crack nucleates and advances from one edge of the lattice. This failure mechanism was also predicted in the finite element (FE) simulations of elastic-brittle PMMA lattices by assuming a local tensile strain failure criterion. Furthermore, both the measured and predicted macroscopic strength of a lattice of finite specimen geometry agree with the analytical predictions of Gibson and Ashby [1]. The strength of the brittle lattice is sensitive to the presence of as-designed defects in the form of missing cell walls¹ and it is relatively insensitive to the presence of filled cells and randomly misplaced joints. The aim of the present study is to determine whether similar conclusions can be drawn for a lattice deforming in the creep regime. For example, is the degree of imperfection sensitivity in the creep regime significantly less than that in the elastic-brittle regime?

1.2. The creep response of foams and honeycombs

At elevated temperature T close to T_g for polymers, or T exceeding 30% of the absolute melting temperature T_m for metals and ceramics, foams undergo time-dependent plastic flow, or *creep*. Gibson and Ashby [1] have considered the case of a foam with cell walls that undergo power-law creep, such that the uniaxial strain rate $\dot{\epsilon}$ of the solid scales with the tensile stress σ according to

$$\dot{\epsilon} = \dot{\epsilon}_s \left(\frac{\sigma}{\sigma_s} \right)^{n_s} \quad (3)$$

in terms of the material constants $\dot{\epsilon}_s$, σ_s , and the creep exponent n_s . The creep exponent of the honeycombs or foams inherits its value from that of the parent solid, as explained by Boccaccini et al. [14]. Gibson and Ashby [1] predict that the macroscopic creep rate $\dot{\epsilon}^\infty$ of an open-cell foam scales with the macroscopic tensile stress

¹The removal of cell walls leads to a shift in behaviour from strength control to K -dominated behaviour at a small transition flaw size a_T on the order of 1 cell size.

σ^∞ according to

$$\frac{\dot{\varepsilon}^\infty}{\dot{\varepsilon}_s} = \frac{0.6}{(n_s + 2)} \left(\frac{1.7(2n_s + 1)}{n_s} \frac{\sigma^\infty}{\sigma_s} \right)^{n_s} \left(\frac{1}{\bar{\rho}} \right)^{(3n_s + 1)/2} \quad (4)$$

The dependence of creep rate upon relative density, as stated in Eq. (4), has been confirmed experimentally for open-cell metallic [2] and ceramic foams [11]. The creep parameters of polymeric foams also inherit their values from those of the parent solid; for example, Huang and Gibson [9] found that the creep activation energy of foamed polystyrene equals that of the solid. The visco-elastic response of open and closed-celled polymer foams has been studied in the low-temperature regime [4–6, 9] whereas the present study addresses the high-temperature visco-plastic, creep response of polymer honeycombs at temperatures close to the glass transition temperature, T_g .

It is broadly accepted that the power-law creep response of honeycombs and foams is sensitive to the presence of missing cell walls [10, 15], to a dispersion in cell wall thickness [16], to the existence of randomly misplaced joints [16], and Plateau borders [12, 17]. The emphasis of the present study differs from that of previous work on the creep of polymeric foams: our aim is to explore the sensitivity of failure mechanisms (localised versus diffuse), and associated strength and ductility, to the presence of geometric and material imperfections.

1.3. Scope of study

The purpose of the current study is to examine experimentally the deformation and fracture responses of two-dimensional (2D), visco-plastic, hexagonal honeycombs made by rapid prototyping. The honeycombs were cut from polymethyl methacrylate (PMMA) sheets and the macroscopic stress versus strain response was measured for uniaxial tension at fixed strain rate, in a temperature-controlled chamber at 100 °C which is close to the glass transition temperature T_g of PMMA. The as-manufactured lattice geometry contains Plateau borders and strut thickness variation. The magnitude of these 2 defects was measured by computer-assisted tomography (CT). Finite element (FE) predictions of the macroscopic stress versus strain response were made on the basis of (i) the measured geometry from the CT-scans, (ii) the measured visco-plastic response of a single strut, and (iii) the measured dispersion of strut ductility associated with the manufacturing method. The notion of a transition flaw size is used to quantify the sensitivity of lattice strength to defect size. Irregular lattices were

also created by the introduction of as-designed defects, specifically a centre crack (due to missing cell walls), solid inclusions in the form of filled cells, and randomly perturbed joints. The knock-down in lattice strength due to each of these defects was measured.

2. Experimental investigation

The experimental procedure, including the manufacturing parameters for laser-cutting the PMMA sheets, has already been detailed in the companion study [13]. The same manufacturing routine was applied in this study, along with the same material batch of cast 5 mm thick PMMA sheets. In brief, specimens were manufactured by laser-cutting² into the following 5 geometries:

- (i) single strut specimen, as shown in Fig. 1(a), for material characterisation on a small scale;
- (ii) regular hexagonal lattice, as shown in Fig. 1(b), to measure the lattice response, absent as-designed defects;
- (iii) irregular hexagonal lattice containing as-designed defects in the form of (a) randomly perturbed joints, (b) missing cell walls, or (c) solid inclusions, see Fig. 2.

The dispersion in strut thickness t and in Plateau border radius r for lattice specimens of types (ii) and (iii) have already been characterised by X-ray computed tomography (CT) in Ref. [13]. Both t and r are defined in Fig. 1(b). The strut thickness was measured at mid-length of 453 struts. It follows a normal distribution with a mean value $\bar{t} = 0.47$ mm, where the overbar throughout this study denotes the average value (with the exception of density for which an overbar denotes relative density). The standard deviation of the strut thickness is $t_{\text{sd}} = 0.09$ mm. The Plateau border radius was quantified by a measured mean value $\bar{r} = 0.4$ mm and standard deviation $r_{\text{sd}} = 0.1$ mm.

For lattice specimens of type (ii), the relative density of the lattice $\bar{\rho}$ is varied from 0.07 to 0.19 by varying the strut length ℓ from 3.0 mm to 7.5 mm. The PMMA employed in this study has a glass transition temperature³ $T_g = 385$ K. All specimens were tested at $T = 100$ °C = $0.97 T_g$.

²HPC Laser Ltd LS6090 Pro 80 Watt laser cutter; process parameters: 8 mm/s cutting speed, 60% power, 55% corner power.

³The value of T_g was measured by Dynamic Mechanical Analysis (DMA) of a single PMMA cantilever beam at an excitation frequency equal to 0.1 Hz and a heating rate of 5 °C/min, refer to [18] for details of the test procedure.

3. Manufacture of lattice specimens and test method

A computer-aided drawing (CAD) of the geometry of a regular hexagonal lattice, as shown in Fig. 1(b), was created using the *OpenSCAD*⁴ software. This CAD file provides an input to the laser cutting machine with sufficient data to define the translation of the cutting head relative to a fixed position on the PMMA sheet. The hexagonal lattices were manufactured to dogbone shape in order to ensure that failure occurs within the gauge section, see Fig. 1(b). All lattice specimens have a gauge width $W = 11\sqrt{3}\ell$ (or 11 cells) and a gauge length $L = 11\ell$ (or 7 cells). The front and back faces of the end, gripping portions of the lattice specimens were adhered to 2 mm thick aluminium alloy end tabs, see Fig. 1(b).

All lattice specimens were tested in uniaxial tension using a servo hydraulic test machine at a nominal strain rate of $\dot{\epsilon} = 4 \times 10^{-4} \text{ s}^{-1}$. The tests were conducted at 100 °C in a temperature-controlled chamber with a glass window for in-situ observation of the specimen during the test. The temperature was maintained to a precision of $\Delta T \pm 2 \text{ K}$ during each test. The load P was measured via a load cell clamped to the stationary platen of the rig while the extension u of the gauge length was determined by Digital Image Correlation (DIC), as described in [13]. Prior to the start of each test, the lattice specimens were coated with a thin layer of white chalk, and a speckle pattern was generated by the spraying of black paint in order to enhance the contrast of the DIC imagery. A digital camera⁵ was used to track facets of size 20×20 pixels in the vicinity of all nodes to enable sub-pixel resolution of the nodal displacement.

4. Material characterisation

The as-manufactured material properties of solid PMMA were measured from the tensile response of laser-cut single strut specimens of mean strut thickness $\bar{t} = 0.47 \text{ mm}$ and strut length $L_s = 10 \text{ mm}$. The tests were conducted at 100 °C in a temperature-controlled chamber as described before. The extension of the single strut specimens was measured by optical tracking of white dots at the ends of the gauge length along the centre-line of the specimen using DIC technique.

⁴<https://www.openscad.org>

⁵maximum resolution: 4608×3288 pixels, 55 mm lens for lattices and 100 mm lens for single strut tests

The measured nominal stress versus nominal strain response for 3 different strain rates within the range $4 \times 10^{-4} \text{ s}^{-1}$ to $4 \times 10^{-3} \text{ s}^{-1}$ are shown in Fig. 3. The flow strength increases with increasing strain rate. Negligible necking was found at 100°C due to the visco-plastic material behaviour which is in agreement with the observations of Van Loock and Fleck [18]. The single strut has a nominal failure strain ε_{fs} of 2.5, or equivalently, a true failure strain of 1.3. The single strut failure strain is insensitive to strain rate over the range tested.

5. Measured tensile response of as-manufactured lattice specimens

The measured macroscopic nominal stress σ^∞ versus nominal strain ε^∞ responses of 3 lattice specimens of Fig. 1(b) are shown in Fig. 4(a). Each specimen contains 453 struts of length $\ell = 5 \text{ mm}$. Representative curves are shown for a single specimen at each relative density of $\bar{\rho} = 0.07, 0.11, \text{ and } 0.19$. The macroscopic nominal quantities σ^∞ and ε^∞ are defined in terms of the measured load P and the extension u of the gauge length as $\sigma^\infty = P/(WB_0)$ and $\varepsilon^\infty = u/L$, respectively. The dimensions (W, L) are defined in Fig. 1(b); W equals 96 mm, L equals 55 mm, and the out-of-plane thickness B_0 equals 5 mm.

The sequence of strut failure in a lattice specimen of relative density $\bar{\rho} = 0.11$ is shown in Fig. 4(a), with the corresponding locations of strut failure marked in Fig. 4(b). The following observations are made from Figs. 4(a) and (b), and are representative of the response for all 3 values of $\bar{\rho}$. All failed struts exist within the gauge section of the specimen and strut failure occurs always close to a joint. First strut failure does not necessarily occur at the edge of the specimen. Subsequent strut failures occur at random locations, leading to a diffuse mode of damage, see Fig. 4(b). First strut failure is accompanied by only a small drop in the load P (and in turn σ^∞). The cell wall solid has a sufficiently high strain-rate hardening response that the macroscopic stress σ^∞ is almost constant during the progressive failure of the first 6 struts at random locations within the lattice. Approximately 50% of the failed struts are inclined at $\pm 60^\circ$ to the loading axis in the undeformed configuration. In contrast, 90% of the failed struts of elastic-brittle PMMA lattices were inclined at $\pm 60^\circ$ to the loading axis [13]. It is appreciated that this specimen is not sufficiently long in order to give the response of an infinite domain of lattice material. The large Poisson contraction and large tensile strain ($\varepsilon^\infty \approx 1$) exhibited by the specimen lead to a non-uniform stress state. This is difficult to overcome in an experimental manner:

a specimen of gauge width on the order of 100 cells (or 1 m) would be needed to give a uniform stress state. Thus, an alternative strategy of modelling was employed: the full specimen was analysed by finite element simulations in order to make predictions, instead of the periodic cell calculations.

It is instructive to compare the strut nominal ductility e_f with the nominal failure strain of the cell wall solid $\bar{\epsilon}_{fs}$, as follows. The nominal axial strain e of each strut was measured in the gauge section of the specimens, and the axial failure strain e_f of each strut was recorded just prior to the strut failure. This failure strain e_f is the nominal value over the length of a strut, as measured from the centre point of the joints at each end of the failed strut. This definition is shown in the inset of Fig. 5. A wide dispersion in strut ductility e_f was observed in both the inclined and aligned struts with regard to the loading direction. To illustrate this, the measured value of e_f was plotted as a function of macroscopic nominal strain ϵ^∞ in Fig. 5. The data from 3 nominally identical specimens are shown, for each value of $\bar{\rho}$. The strut ductility e_f approaches the value of $\bar{\epsilon}_{fs} = 2.5$ at a macroscopic nominal strain ϵ^∞ exceeding 0.8.

6. Simulations

6.1. Details of the FE model

The finite element (FE) method is used to investigate numerically the tensile creep response of PMMA lattices made from rapid prototyping. The main objective of the FE study is to examine the sensitivity of the macroscopic response to as-manufactured defects such as the dispersion in strut thickness, Plateau border radius, and strut ductility. Two geometries of lattice specimen of relative density $\bar{\rho} = 0.11$ are modelled explicitly for comparison with the experimental observations: (i) an ideal lattice with constant strut thickness and constant Plateau border radius, and (ii) structural realisations of the as-manufactured lattice, as shown in Fig. 6, for direct comparison with the experimental observations. The specimen geometry was scanned by CT and the FE mesh was constructed using the centre plane of the scanned geometry. The struts within the lattice have a variable thickness, with a mean value of $\bar{t} = 0.47$ mm and a standard deviation of $t_{sd}/\bar{t} = 0.19$. Quasi-static calculations were performed with ABAQUS/Explicit v6.14 to simulate the deformation and failure response of these specimens under remote uniaxial tensile loading.

The FE mesh comprises quadratic triangular elements in plane strain (type CPE6M) of uniform size ℓ_e such that the thinnest strut in the lattice has at least five elements across its thickness, and the stress concentration at the Plateau borders is adequately captured, as shown in the inset of Fig. 6(a). Uniaxial loading of the specimen is simulated by constraining all degrees of freedom along the bottom edge of the specimen ($u_1 = u_2 = 0$) while the top edge is displaced in the x_2 -direction of the specimen ($u_1 = 0, u_2 = u$), see Fig. 6(a).

6.1.1. Material model

The cell wall material is modelled as an elastic, visco-plastic solid. Tensile fracture of the individual struts of the lattice is simulated using an idealised Johnson-Cook type continuum damage mechanics approach. This approach assumes that damage initiates in accordance with a local strain criterion whereas damage evolves on the basis of a prescribed work of fracture. A detailed explanation of the material model assumed in the FE simulations is given below.

The cell wall has a Young's modulus $E_s = 400$ MPa and Poisson's ratio $\nu_s = 0.3$, as measured from the single strut specimens. We adopt a visco-plastic constitutive law in terms of the true plastic strain ε^P , true stress σ , and strain rate $\dot{\varepsilon}$. It has the form

$$\sigma = \sigma_0 \sinh^{-1} \left(\frac{\dot{\varepsilon}}{\dot{\varepsilon}_0} \right) f(\varepsilon^P) \quad (5)$$

where the reference values $(\sigma_0, \dot{\varepsilon}_0)$ are taken as $\sigma_0 = 1$ MPa and $\dot{\varepsilon}_0 = 4.4 \times 10^{-6} \text{ s}^{-1}$ such that $\sigma(\dot{\varepsilon}, \varepsilon^P = 0) = 5.2$ MPa, 6.1 MPa and 7.5 MPa for the 3 values of strain rate $\dot{\varepsilon} = 4 \times 10^{-4} \text{ s}^{-1}$, 10^{-3} s^{-1} and $4 \times 10^{-3} \text{ s}^{-1}$, respectively. It remains to specify $f(\varepsilon^P)$ in Eq. (5). A curve-fitting procedure is carried out on the measured σ versus ε^P data excluding the initial peak and the subsequent softening characteristics of Fig. 3. This procedure results in the following functional form for $f(\varepsilon^P)$:

$$f(\varepsilon^P) = \begin{cases} \exp(0.9\varepsilon^P) & \text{for } 0 \leq \varepsilon^P < 0.6 \\ 0.835 \exp(1.2\varepsilon^P) & \text{for } 0.6 \leq \varepsilon^P < 0.92 \\ 0.48 \exp(1.8\varepsilon^P) & \text{for } \varepsilon^P \geq 0.92 \end{cases} \quad (6)$$

Following Johnson and Cook [19], it is assumed that damage at a material element (i.e. integration point)

initiates when the equivalent plastic tensile strain at that point attains the solid tensile ductility, ε_{fs} , as indicated in Fig. 6(b). A deterministic value of strut ductility (i.e. true strain to failure), $\varepsilon_{fs} = 1.3$, is assumed for all struts in the lattice taken from the measured mean ductility of single strut specimens, recall Fig. 3.

The subsequent *evolution* of damage at a material point is specified via a linear softening σ versus ε^P relationship given by

$$\sigma = \sigma_f \left(1 - \frac{\varepsilon^P - \varepsilon_{fs}}{\Delta\varepsilon} \right) \quad (7)$$

where σ_f is the stress level at $\varepsilon^P = \varepsilon_{fs}$ as given by Eq. (6), and $\Delta\varepsilon$ is the plastic strain increment over the softening portion of the response, see Fig. 6(b). The value of $\Delta\varepsilon$ follows from the specified work of fracture in the softening regime, Γ_f , and the characteristic length associated with the finite element, ℓ_c , as: $\Delta\varepsilon = 2\Gamma_f/\sigma_f\ell_c$. Note that $\ell_c = \ell_e/2$ for quadratic triangular finite elements. A value of $\Gamma_f = 2.5 \text{ kJ/m}^2$ is assumed in the current FE simulations upon making use of the Irwin relation $\Gamma_f = K_{IC}^2/E_s$ with $K_{IC} = 1 \text{ MPa}\sqrt{\text{m}}$ as taken from [20] and $E_s = 400 \text{ MPa}$ from the single strut experiments. It is noted that the specification of damage evolution via Eq. (7) in terms of the size of the finite element alleviates the problem of mesh size dependence of the solution; refer to Ref. [21] for details. We emphasise that this Johnson-Cook type failure model gives rise to strut failure in a combined stretching and bending manner at a location near the joints. This is in agreement with the observed nature of strut failure.

6.2. FE predictions of the tensile response of as-manufactured lattice specimens

In order to quantify the role of as-manufactured defects, such as the variation in strut thickness and in Plateau border radius, baseline FE simulations were performed on a lattice of a uniform strut thickness t , Plateau border radius r , and a deterministic value of cell wall ductility ε_{fs} . Accordingly, the predicted response of a perfect lattice specimen of relative density $\bar{\rho} = 0.11$ is shown in Fig. 7(a) for $t = \bar{t} = 0.47 \text{ mm}$ and $r = \bar{r} = 0.4 \text{ mm}$ and a true failure strain $\varepsilon_{fs} = 1.3$ for all struts in the lattice. The measured response of one of the as-manufactured specimens of $\bar{\rho} = 0.11$ is included in Fig. 7(a) for comparison. We find from Fig. 7(a) that the initial stiffness of the lattice is predicted accurately by the perfect geometry, implying a negligible effect of the geometric imperfections on the elastic stiffness of the lattice. The first strut to fail in the perfect lattice does so at a

macroscopic nominal strain of 0.76, which significantly exceeds the measured nominal strain at first strut failure of 0.18. The predicted macroscopic strength of the perfect lattice also exceeds the measured value.

The sensitivity of macroscopic strength to the presence of as-manufactured defects is explored by performing an FE simulation on the geometry of the as-manufactured specimen as defined from a CT scan of the mid-plane section. This geometry contains a dispersion in strut thickness and in Plateau border radius as specified by $t_{sd}/\bar{t} = 0.19$ and $r_{sd}/\bar{r} = 0.25$, respectively. A deterministic value of cell wall ductility $\varepsilon_{fs} = 1.3$ is again assumed for all struts in the lattice such that $\varepsilon_{fs,sd} = 0$. The predicted response of the as-manufactured specimen shows early strut failure at a macroscopic nominal strain of 0.42 and a macroscopic strength slightly above the measured value, see Fig. 7(a). The failure of struts in the FE simulations for both the perfect and as-manufactured geometries occurs in a correlated crack-like manner as shown in Fig. 7(b). This contrasts with the observed diffuse damage mode. We proceed to show that the diffuse damage mode requires a dispersion in strut ductility.

6.2.1. Effect of a dispersion in strut ductility

The distribution of measured strut nominal ductility e_f is re-plotted in Fig. 8 in the form of a probability distribution curve $p(e_f)$, based on the data from Fig. 5. The measured distribution fits a Gaussian distribution of mean value $\bar{e}_f = 1.63$ and standard deviation $e_{sd}/\bar{e}_f = 0.4$. Is this observed distribution in strut ductility due to the imperfect geometry of the lattice (i.e. dispersion in t and r) or is it due to the scatter in material ductility from one strut to the next? In order to address this, a set of 5 FE simulations were performed, all based on the same mesh (as defined by the CT measurement). However, each simulation assumed a different realisation of randomly-generated strut ductility ε_{fs} in accordance with the normal distribution curve of $\bar{\varepsilon}_{fs} = 1.3$ and $\varepsilon_{fs,sd}/\bar{\varepsilon}_{fs} = 0.4$. Note that the assumed value of $\bar{\varepsilon}_{fs}$ equals the measured value of single strut ductility from Fig. 3. The assumed value of $\varepsilon_{fs,sd}/\bar{\varepsilon}_{fs}$ is taken to equal the measured value $e_{f,sd}/\bar{e}_f$ of strut ductility from Fig. 8. The predicted σ^∞ versus ε^∞ response of one of the 5 structural realisations is shown in Fig. 7(c), along with the measured response of this specimen. We find from Fig. 7(c) that an assumed dispersion in strut ductility leads to the early failure of some struts, consistent with experimental observations. The first strut fails at the edge of the specimen at a nominal macroscopic strain of $\varepsilon^\infty = 0.18$; this strut is of thickness $t = 0.3$ mm

and ductility $\varepsilon_{fs} = 1.03$. Subsequent strut failure in the FE simulation occurs at random locations within the lattice. At $\varepsilon^\infty = 1$, the size of the cluster of failed struts approaches the half width of the specimen and macroscopic stress drops to 30% of the value at first strut failure. The sequence and location of strut failure for the assumed distribution $\varepsilon_{fs,sd}/\bar{\varepsilon}_{fs} = 0.4$ is shown in Fig. 7(b): the mode of damage is diffuse in nature, and in good agreement with the experimental observations.

Each FE simulation also gives rise to a sequence of failed struts under increasing macroscopic nominal strain ε^∞ . The predicted strut nominal ductility e_f of each failed strut (from the 5 simulations) is plotted in the form of a probability distribution curve in Fig. 8. It is in excellent agreement with the observed distribution, implying that the assumed scatter in material failure strain $\varepsilon_{fs,sd}/\bar{\varepsilon}_{fs} = 0.4$ is of the correct level. The strong influence of the dispersion in material ductility from one strut to the next on the creep response of the lattice becomes evident upon comparing the predicted probability distribution of e_f of the same lattice geometry, but with a deterministic value of strut ductility ($\bar{\varepsilon}_{fs} = \varepsilon_{fs} = 1.3$ and $\varepsilon_{fs,sd} = 0$), as shown in Fig. 8: presence of geometric imperfections alone (i.e. dispersion in t and r) in the FE mesh leads to a narrow distribution in $p(e_f)$. We conclude that a dispersion in strut ductility is essential to lead to early strut failure and diffuse damage prior to catastrophic fracture of the lattice, as observed in the experiments. In the following section, a discussion is given of the required material properties that govern the competition between a diffuse and a correlated mode of strut failure: the primary properties are the dispersion in strut ductility and the transition flaw size.

6.3. Damage tolerance in creep regime

The transition flaw size is a useful parameter for quantifying the flaw sensitivity of a lattice. It is the minimum semi-length of a centre-crack for which catastrophic failure is dictated by the fracture toughness K_{IC} of the lattice rather than the tensile strength of the uncracked lattice. The notion of a transition flaw size was explored for the case of a brittle lattice by Fleck and co-workers [13, 22, 23] and for the case of a ductile lattice by Tankasala et al. [24]. In all cases, the transition flaw size a_T is given by

$$a_T \approx \frac{1}{\pi} \left(\frac{K_{IC}}{\sigma_f^\infty} \right)^2 \quad (8)$$

where K_{IC} is the macroscopic mode I fracture toughness of the lattice, and σ_f^∞ is the macroscopic tensile strength for a brittle lattice, or the macroscopic yield strength for a ductile lattice. The transition flaw size is on the order of one unit cell dimension ($a_T \approx \ell$) for a brittle hexagonal lattice for which each strut fails by bending. In contrast, the struts of a ductile hexagonal lattice fail by stretching, and consequently, $a_T \approx 250\ell$, following the predictions of Tankasala et al. [24] for $\varepsilon_{fs} = 1.3$ in the absence of cell wall strain hardening. Four classes of lattice behaviour can be identified, depending upon the values of a_T/ℓ and $\varepsilon_{fs,sd}/\bar{\varepsilon}_{fs}$, see Fig. 9(a):

- (i) *Case A* is a brittle hexagonal lattice with a deterministic value of strut tensile strength (or ductility) such that $\varepsilon_{fs,sd} = 0$. Cell walls within the lattice fail at a local bending strain of only a few percent, giving rise to $a_T \approx \ell$. PMMA lattices at room temperature can behave in this manner, see for example Seiler et al. [13].
- (ii) *Case B* is a ductile hexagonal lattice with a deterministic value of strut ductility ($\varepsilon_{fs,sd} = 0$). When failure of a cell wall is dictated by the average tensile strain across a section of the strut, then the transition flaw size of the lattice is on the order of few hundreds of cells, $a_T \approx 250\ell$ for a perfectly plastic cell wall solid of $\varepsilon_{fs} = 1.3$ as previously reported by Tankasala et al. [24].
- (iii) *Case C* is a ductile hexagonal lattice with a dispersion in strut ductility such that $\varepsilon_{fs,sd}/\bar{\varepsilon}_{fs} = 0.4$. Similar to case B, the transition flaw size is of order $a_T \approx 250\ell$ when the average tensile strain across a section of the strut dictates strut failure. The PMMA lattices of the current study (tested at 100°C) belong to this category.
- (iv) *Case D* is a brittle hexagonal lattice with a dispersion in strut tensile strength (or ductility) such that $\varepsilon_{fs,sd}/\bar{\varepsilon}_{fs} = 0.4$. PMMA lattices at room temperature can also be of this class, and possess a small $a_T \approx \ell$, as confirmed recently by Seiler et al. [13].

The above cases A through D are summarised in Fig. 9(a). Seiler et al. [13] have shown by a combination of experiment and FE analysis on PMMA lattices at room temperature that the sequence of strut failure in brittle lattices of type A and D is correlated, as sketched in Fig. 9(b). When the failure strain of a strut is deterministic (case A), the most highly stressed strut fails first, and then the adjacent struts fail in a sequential, correlated

manner. A dispersion in the strut ductility of the lattice (case D) leads to failure of struts at random locations within the lattice, but a small transition flaw size $a_T \approx \ell$ again leads to a correlated failure mode of struts adjacent to the weakest one.

In contrast, the transition flaw size a_T is large compared to the strut length of PMMA lattices at high temperature (100°C), and failure is either correlated (case B) or diffuse (case C) depending upon the value of $\varepsilon_{fs,sd}/\bar{\varepsilon}_{fs}$. Consider first the case of a deterministic strut failure strain, $\varepsilon_{fs,sd} = 0$, case B. A crack-like damage zone develops such that failure of most highly stressed strut triggers the creep failure of adjacent struts: a correlated damage zone develops. Alternatively, a high value of $\varepsilon_{fs,sd}/\bar{\varepsilon}_{fs}$, such as $\varepsilon_{fs,sd}/\bar{\varepsilon}_{fs} = 0.4$, leads to a diffuse mode of damage. Final fracture occurs when the size of a critical cluster of failed struts exceeds the least of $2a_T$ and $0.5W$; this is shown in case C of Fig. 9(b). The approximate position of the boundary between diffuse and correlated modes of damage is shown in Fig. 9(a) based on the available data. A much more detailed and exhaustive study is needed to give the precise location of this boundary.

The damage tolerance of a lattice can be assessed, alternatively, by plotting the normalised macroscopic stress σ^∞ versus number of failed struts, n , across the width of the lattice. Here, $\bar{\sigma}_1^\infty$ is the mean macroscopic strength for first strut failure from 5 FE simulations and 3 experiments. Cases A through D are plotted in Figs. 9(c) and (d) from both the experiments and FE. The results for cases A and D are taken from Ref. [13], whereas cases B and C are from the present study. Recall that case C denotes a diffuse mode of strut failure and a large value of a_T . The macroscopic stress σ^∞ drops slightly with an increasing number n of failed struts, see Fig. 9(d). In contrast, the drop in σ^∞ with increasing n follows the net section prediction, $\sigma^\infty/\bar{\sigma}_1^\infty = 1 - (n - 1)/(N - 1)$, for case B of deterministic strut ductility ($\varepsilon_{fs,sd}/\bar{\varepsilon}_{fs} = 0$). Here N is the total number of struts in the gauge section; N equals 12 in Figs. 9(c) and (d). This suggests that a dispersion in strut ductility is beneficial for the enhancement of damage tolerance in the creep regime.

7. The effect of as-designed defects on macroscopic properties: experiment

Three types of macroscopic defect were introduced within the regular lattice by design: (i) misplaced joints, (ii) cells filled with solid inclusions, and (iii) missing cell walls. The resulting as-manufactured specimens contain

geometric and material imperfections at the cell wall level (variation in strut thickness, in Plateau border radius, and in strut ductility) in addition to one of the three macroscopic defects, see Fig. 2. The macroscopic tensile strength at first strut failure of the as-manufactured specimens was measured experimentally at 100°C and a strain rate of $4 \times 10^{-4} \text{ s}^{-1}$ and then compared with that of the as-manufactured topologies designed without macroscopic defects. The sensitivity of measured creep strength to the presence of as-designed defects was thereby assessed.

7.1. Randomly perturbed joints

The effect of cell wall misalignment on the macroscopic creep response of PMMA lattices was investigated by generating imperfect lattice topologies with randomly perturbed joints. These lattices were laser-cut based on a CAD file wherein the joints of a regular hexagonal lattice (of $\bar{\rho} = 0.11$) were repositioned randomly within a circular disc of radius R , following the procedure of Romijn and Fleck [25]. The degree of imperfection was varied by selecting values of R/ℓ between 0 (regular lattice) and 0.5 (extremely imperfect lattice). A typical realisation of the as-manufactured lattice, for the choice $R/\ell = 0.5$, is shown in Fig. 2(a); only those joints which lie within the gauge section were misplaced. The random misplacement of the joints reduces the average strut length such that the relative density of the lattice increases by a factor of 1.0025 for $R/\ell = 0.1$ and by a factor of 1.0625 for $R/\ell = 0.5$, as previously noted by Romijn and Fleck [25]. This minor change in $\bar{\rho}$ is ignored in the current study.

The sensitivity of macroscopic tensile strength σ_f^∞ at first strut failure, and macroscopic tensile ductility ε_f^∞ at first strut failure, to random perturbation of joints was measured for 3 structural realisations for each choice of $R/\ell = 0, 0.3$, and 0.5, all for relative density $\bar{\rho} = 0.11$. The measured values of σ_f^∞ and ε_f^∞ are plotted in Fig. 10 as a function of the degree of imperfection R/ℓ . The ordinate in each case is normalised by its corresponding mean value as measured for the regular lattice ($R/\ell = 0$). For comparison, the knock-down in σ_f^∞ with increasing R/ℓ for the case of elastic-brittle PMMA lattices (of $\bar{\rho} = 0.11$) is included in Fig. 10. The mean values of σ_f^∞ are obtained from 3 realisations.

No significant knock-down in macroscopic tensile strength and macroscopic tensile ductility was found for $0 < R/\ell \leq 0.3$. Significant scatter in both σ_f^∞ and ε_f^∞ is observed when R/ℓ is increased from 0.3 to 0.5. The

mean values of σ_f^∞ and ε_f^∞ are reduced by a factor of 2 and 1.6, respectively, from $R/\ell = 0.3$ to $R/\ell = 0.5$. This knock-down in σ_f^∞ and ε_f^∞ is attributed to the development of discrete force chains spanning the length of the specimen, wherein the struts deform predominantly by stretching. This observation is consistent with the FE predictions of Tankasala et al. [24] which revealed that few force chains in the lattice carry most of the applied load, and the stretching-dominated failure of these struts results in a reduction of the macroscopic ductility. The sequence of strut failure in a representative specimen of $R/\ell = 0.5$ in Fig. 10(c) reveals a diffuse mode of damage, similar to the $R/\ell = 0$ case. For all realisations of $R/\ell > 0$ tested in this study, first strut to fail is always located at the centre of the specimen.

7.2. Missing cell walls

A centre-crack was introduced in regular lattice specimens by removing a row of cell walls: the cell walls comprising the crack were first heated by a soldering iron. They were then cut whilst the deformation response of the PMMA strut was in the rubbery regime, to obtain specimen geometry as sketched in Fig. 2(b). The initial crack is of semi-length $a_0 = \sqrt{3}n_b\ell/2$ where n_b is the number of broken cell walls. The influence of crack length on the tensile strength of the lattice was explored by varying n_b between 0 and 6; 3 realisations of the lattice were generated for each value of n_b , with $\bar{\rho} = 0.11$.

The sensitivity of macroscopic tensile strength σ_f^∞ at first strut failure to the presence of a macroscopic crack is shown in Fig. 11(a) as a function of the crack length a_0/ℓ . As before, the ordinate in Fig. 11(a) is normalised by its corresponding mean value as measured for the uncracked lattice ($a_0/\ell = 0$). The ductile hexagonal lattice has a high transition flaw size a_T such that only a small knock-down in tensile strength is observed for $a_0/\ell \leq 5$. This behaviour is in contrast to the response of centre-cracked brittle PMMA lattices in which the tensile strength was observed to be governed by the fracture toughness of the lattice, see [13] for details. Note that the net section strength of the ductile lattice always lies above the gross section strength, and so the measured strengths of Fig. 11(a) indicate a significant elevation in net section strength at small (but finite) a_0/ℓ . The reason for this strengthening is unclear, and is a topic for future research. The available evidence in the insert of Fig. 11(a) suggests a blunting mechanism at the tip of the pre-crack, whereby the struts align with the loading direction. This crack tip blunting phenomenon has been analysed by Tankasala et al. [26] for the

case of a long crack in a ductile hexagonal lattice. This explanation is also consistent with that of Mangipudi and Onck [27]. They calculated the net section strength of a centre-cracked panel (CCP) of a honeycomb of random Voronoi microstructure. They modelled the failure of each strut by using softening beam elements, and found a small elevation in net section strength when the size of the pre-crack was increased from $a/W = 0$ to $a/W = 0.1$. Mangipudi and Onck [27] noted that the strengthening is associated with a change in fracture path from a random, uncorrelated manner to failure originating from the crack tip. This is consistent with the observed switch in failure path in the present study, compare Fig. 4(b) for $a_0/\ell = 0$ with Fig. 11(c) for $a_0/\ell = 2.6$. For initial cracks of semi-length $a_0/\ell \geq 2.6$, first strut failure occurs near the tip of the macroscopic crack, as shown in Fig. 11(c). Subsequent strut failure occurs in a correlated manner with the advancing crack predominantly comprising of vertical struts.

7.3. Solid inclusions

Hexagonal lattices containing a solid inclusion were generated by the laser-cutting of PMMA sheets, with a number of intact filled cells at the centre of the specimen, recall Fig. 2(c). The semi-length of the inclusion is $a_0 = \sqrt{3}n_c\ell/2$ where n_c is the number of filled cells. Three realisations of the lattice were generated for each value of n_c between 0 and 6, with $\bar{\rho} = 0.11$.

The measured values of macroscopic tensile strength σ_f^∞ at first strut failure are plotted in Fig. 11(b) as a function of the inclusion size a_0/ℓ . The sensitivity of σ_f^∞ to a_0/ℓ for the case of elastic-brittle lattice as taken from Ref. [13] are included in Fig. 11(b) for comparison. A mild increase in σ_f^∞ is observed for increasing values of a_0/ℓ . This is due to a reduction in the lateral contraction of cells in the vicinity of the inclusions. Diffuse strut failure is observed prior to catastrophic fracture with the failed struts not necessarily located in the vicinity of the inclusions, see for example the case of $a_0/\ell = 2.6$ in Fig. 11(d).

8. Concluding remarks

The present study explores the sensitivity of the macroscopic tensile response of a visco-plastic lattice to as-manufactured and as-designed defects. It is found that both classes of defect have a significant effect on the

macroscopic tensile strength of laser-cut PMMA lattices in the visco-plastic regime. FE analysis provides further insight into the relative potency of three types of as-manufactured defect: a dispersion in strut thickness, in Plateau border radius and in strut ductility arising from the manufacturing route.

The evolution of strut failure at T close to T_g is markedly different from that observed at $T < T_g$ in a companion study, Ref. [13]. At room temperature, PMMA behaves in an elastic-brittle manner and the failure of a single strut is sufficient to lead to the formation of a single macroscopic crack in the lattice. In contrast, at $T \approx T_g$, a diffuse zone of failed struts develop prior to catastrophic failure. Finite element analysis reveals that a dispersion in strut-to-strut ductility also plays a major role in giving rise to the diffuse damage state in the creep regime. A dispersion in ductility from strut to strut is essential to give rise to the observed early onset of strut failure as well as the diffuse mode of fracture. The latter in turn enhances the damage tolerance of these lattices in creep regime. In contrast, a dispersion in strut thickness and Plateau border radius have only a mild effect in the creep regime, as confirmed by the FE predictions.

As-designed imperfections were also introduced in the laser-cut lattices. Three kinds of imperfections were explored experimentally: randomly misplaced joints, a row of missing cell walls to create a notch, and a row of filled cells as solid inclusions. The following conclusions can be drawn for each type of defect:

- (i) *Imperfections in the form of randomly perturbed joints.* The macroscopic tensile strength of the lattice is insensitive to random perturbation of joints for low values of R/ℓ between 0 and 0.3. A 50% knock-down in tensile strength is observed when the imperfection is most severe ($R/\ell = 0.5$). The macroscopic ductility decreases with increasing values of R/ℓ due to the formation of discrete force chains. This behaviour is in contrast to brittle hexagonal lattices which are almost insensitive to the presence of randomly perturbed joints.
- (ii) *Imperfections in the form of missing cell walls.* Visco-plastic lattices possess high damage tolerance. The transition flaw size a_T for strength-controlled failure to fracture toughness-controlled failure is sufficiently large such that the macroscopic tensile strength is not reduced by the presence of even 4 missing cells. This observation is consistent with the numerical predictions of Tankasala et al. [24] for ductile hexagonal lattices.

(iii) *Imperfections in the form of solid inclusions.* Lattices with filled cells show a slight increase in tensile strength due to the reduced lateral contraction of cells in the vicinity of the inclusions.

In summary, the macroscopic tensile strength of the visco-plastic hexagonal PMMA lattice is almost insensitive to imperfections in the form of broken cell walls and solid inclusions owing to its high transition flaw size. The random misplacement of joints emerges as the most potent type of defect.

Acknowledgements

The authors gratefully acknowledge the financial support from the European Research Council (ERC) under the European Union's Horizon 2020 research and innovation program, grant GA669764, MULTILAT.

References

- [1] L. J. Gibson, M. F. Ashby, *Cellular solids: structure and properties*, Cambridge University Press, 1999.
- [2] E. W. Andrews, L. J. Gibson, M. F. Ashby, *The creep of cellular solids*, *Acta Materialia* 47 (1999) 2853–2863.
- [3] S. M. Oppenheimer, D. C. Dunand, *Finite element modeling of creep deformation in cellular metals*, *Acta Materialia* 55 (2007) 3825–3834.
- [4] N. J. Mills, A. Gilchrist, *Creep and recovery of polyolefin foams—deformation mechanisms*, *Journal of Cellular Plastics* 33 (1997) 264–292.
- [5] S. Deschanel, L. Vanel, N. Godin, E. Maire, G. Vigier, S. Ciliberto, *Mechanical response and fracture dynamics of polymeric foams*, *Journal of Physics D: Applied Physics* 42 (2009) 214001.
- [6] H. X. Zhu, N. J. Mills, *Modelling the creep of open-cell polymer foams*, *Journal of the Mechanics and Physics of Solids* 47 (1999) 1437–1457.
- [7] Z. G. Fan, C. Q. Chen, T. J. Lu, *Multiaxial creep of low density open-cell foams*, *Materials Science and Engineering: A* 540 (2012) 83–88.
- [8] K. A. Khan, R. K. A. Al-Rub, *Time dependent response of architected Neovius foams*, *International Journal of Mechanical Sciences* 126 (2017) 106–119.
- [9] J. S. Huang, L. J. Gibson, *Creep of polymer foams*, *Journal of Materials Science* 26 (1991) 637–647.
- [10] J. S. Huang, L. J. Gibson, *Creep of open-cell Voronoi foams*, *Materials Science and Engineering: A* 339 (2003) 220–226.
- [11] K. C. Goretta, R. Brezny, C. Q. Dam, D. J. Green, A. R. D. Arellano-Lopez, A. Dominguez-Rodriguez, *High temperature mechanical behavior of porous open-cell Al₂O₃*, *Materials Science and Engineering: A* 124 (1990) 151–158.
- [12] T.-J. Chen, J.-S. Huang, *Creep-rupturing of cellular materials: Regular hexagonal honeycombs with dual imperfections*, *Composites Science and Technology* 68 (2008) 1562–1569.

- [13] P. E. Seiler, H. C. Tankasala, N. A. Fleck, The role of defects in brittle honeycombs made via rapid prototyping, *Acta Materialia* 171 (2019) 190–200.
- [14] D. N. Boccaccini, H. L. Frandsen, B. R. Sudireddy, P. Blennow, Å. H. Persson, K. Kwok, P. V. Hendriksen, Creep behaviour of porous metal supports for solid oxide fuel cells, *International Journal of Hydrogen Energy* 39 (2014) 21569–21580.
- [15] B. Su, Z. Zhou, Z. Wang, Z. Li, X. Shu, Effect of defects on creep behavior of cellular materials, *Materials Letters* 136 (2014) 37–40.
- [16] B. Han, R.-P. Yu, Q.-C. Zhang, H.-J. Gao, Q. Zhang, T. J. Lu, B.-H. Lu, Creep of closed-cell aluminum foams: Effects of imperfections and predictive modeling, *Materials & Design* 156 (2018) 229–241.
- [17] J.-Y. Lin, J.-S. Huang, Creep of hexagonal honeycombs with Plateau borders, *Composite Structures* 67 (2005) 477–484.
- [18] F. Van Look, N. A. Fleck, Deformation and failure maps for PMMA in uniaxial tension, *Polymer* 148 (2018) 259–268.
- [19] G. R. Johnson, W. H. Cook, Fracture characteristics of three metals subjected to various strains, strain rates, temperatures and pressures, *Engineering Fracture Mechanics* 21 (1985) 31–48.
- [20] S. R. Choi, J. A. Salem, Fracture toughness of PMMA as measured with indentation cracks, *Journal of Materials Research* 8 (1993) 3210–3217.
- [21] J. Oliver, A consistent characteristic length for smeared cracking models, *International Journal for Numerical Methods in Engineering* 28 (1989) 461–474.
- [22] N. A. Fleck, X. Qiu, The damage tolerance of elastic–brittle, two-dimensional isotropic lattices, *Journal of the Mechanics and Physics of Solids* 55 (2007) 562–588.
- [23] I. Quintana-Alonso, S. P. Mai, N. A. Fleck, D. C. H. Oakes, M. V. Twigg, The fracture toughness of a cordierite square lattice, *Acta Materialia* 58 (2010) 201–207.
- [24] H. C. Tankasala, V. S. Deshpande, N. A. Fleck, Tensile response of elastoplastic lattices at finite strain, *Journal of the Mechanics and Physics of Solids* 109 (2017) 307 – 330.
- [25] N. E. R. Romijn, N. A. Fleck, The fracture toughness of planar lattices: Imperfection sensitivity, *Journal of the Mechanics and Physics of Solids* 55 (2007) 2538–2564.
- [26] H. C. Tankasala, V. S. Deshpande, N. A. Fleck, 2013 Koiter Medal Paper: Crack-Tip Fields and Toughness of Two-Dimensional Elastoplastic Lattices, *Journal of Applied Mechanics* 82 (2015) 091004.
- [27] K. R. Mangipudi, P. R. Onck, Notch sensitivity of ductile metallic foams: A computational study, *Acta Materialia* 59 (2011) 7356–7367.

Figures

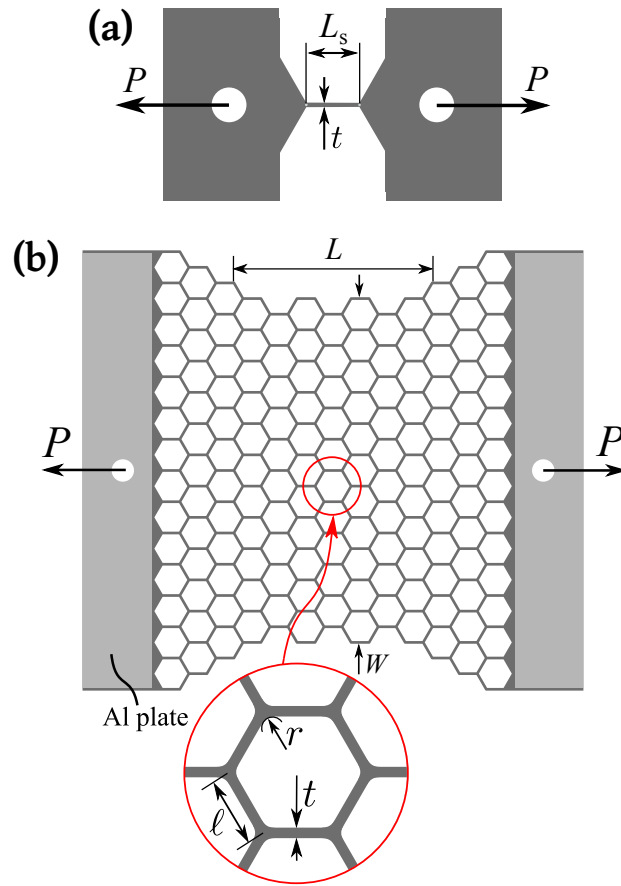


Figure 1: (a) Single strut specimen, and (b) lattice specimen of $\bar{\rho} = 0.11$. The sheet thickness of all samples is $B_0 = 5$ mm.

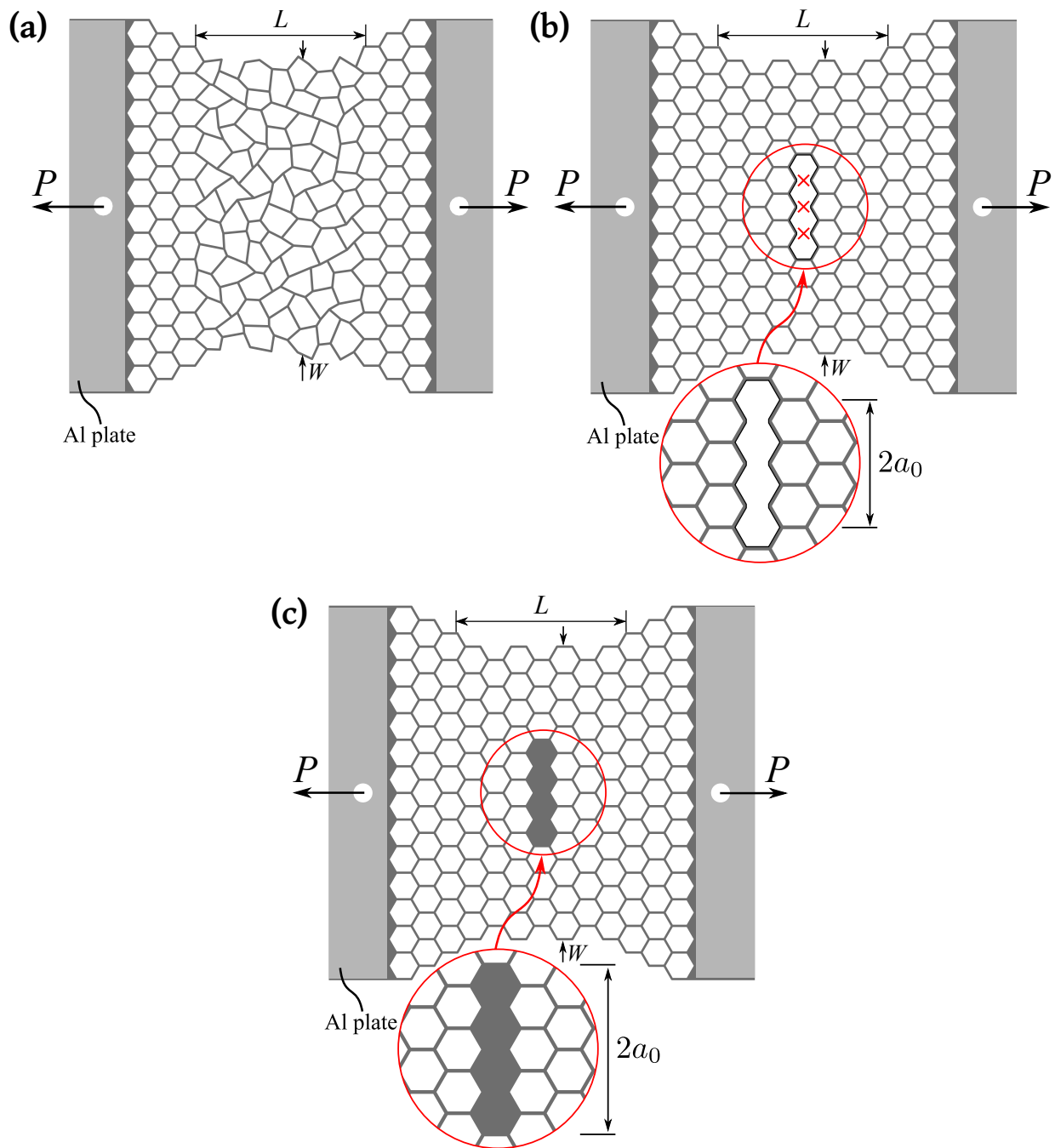


Figure 2: Lattice specimens ($\bar{\rho} = 0.11$) containing as-designed defects in the form of (a) randomly perturbed joints ($R/\ell = 0.5$), (b) a row of missing cell walls, and (c) a row of solid inclusions.

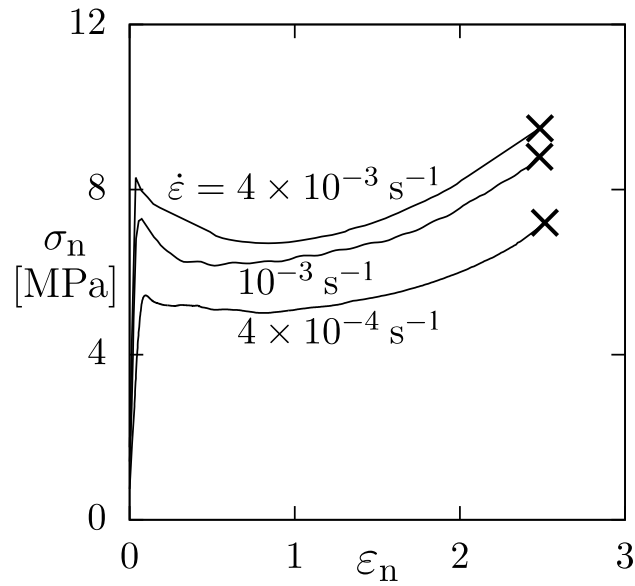


Figure 3: Nominal stress versus nominal strain response of single strut samples at 100 °C, for 3 selected values of strain rate.

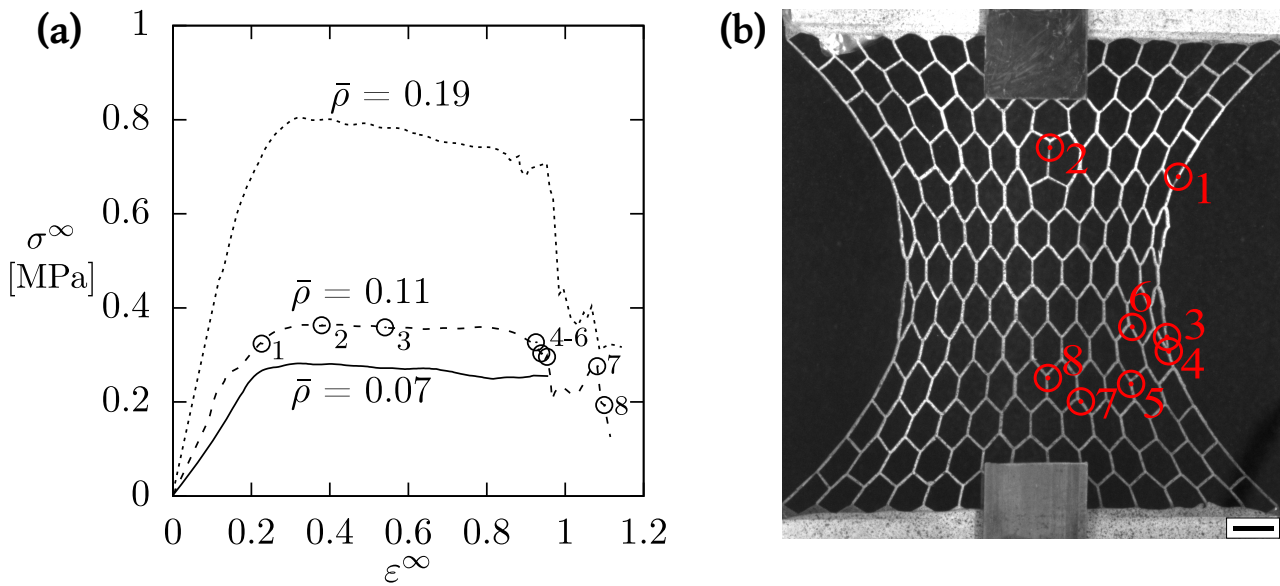


Figure 4: (a) Measured macroscopic nominal stress versus nominal strain response of lattices for selected values of relative density $\bar{\rho}$, (b) deformed lattice ($\bar{\rho} = 0.11$) before first strut failure along with the sequence and location of subsequent strut failure. The scale bar is of length 10 mm.

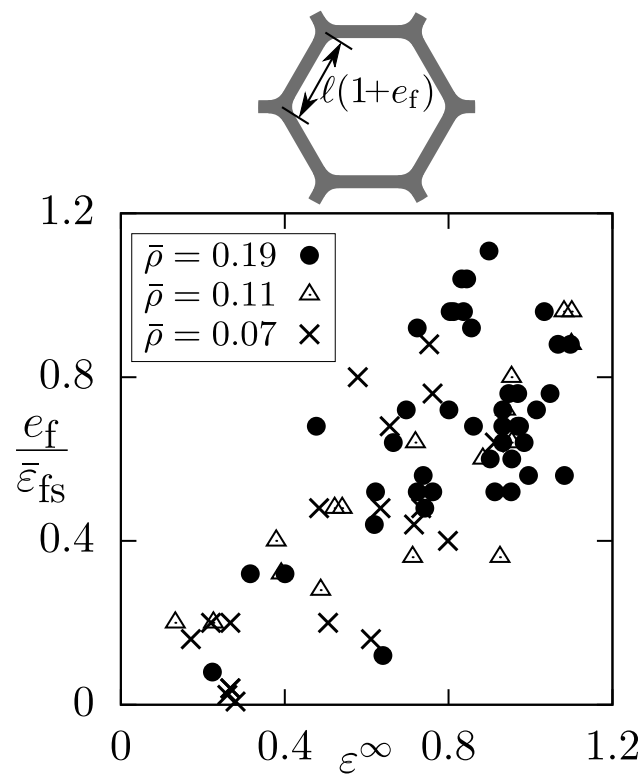


Figure 5: Measured nominal axial failure strain of struts e_f versus the macroscopic nominal strain ϵ^∞ .

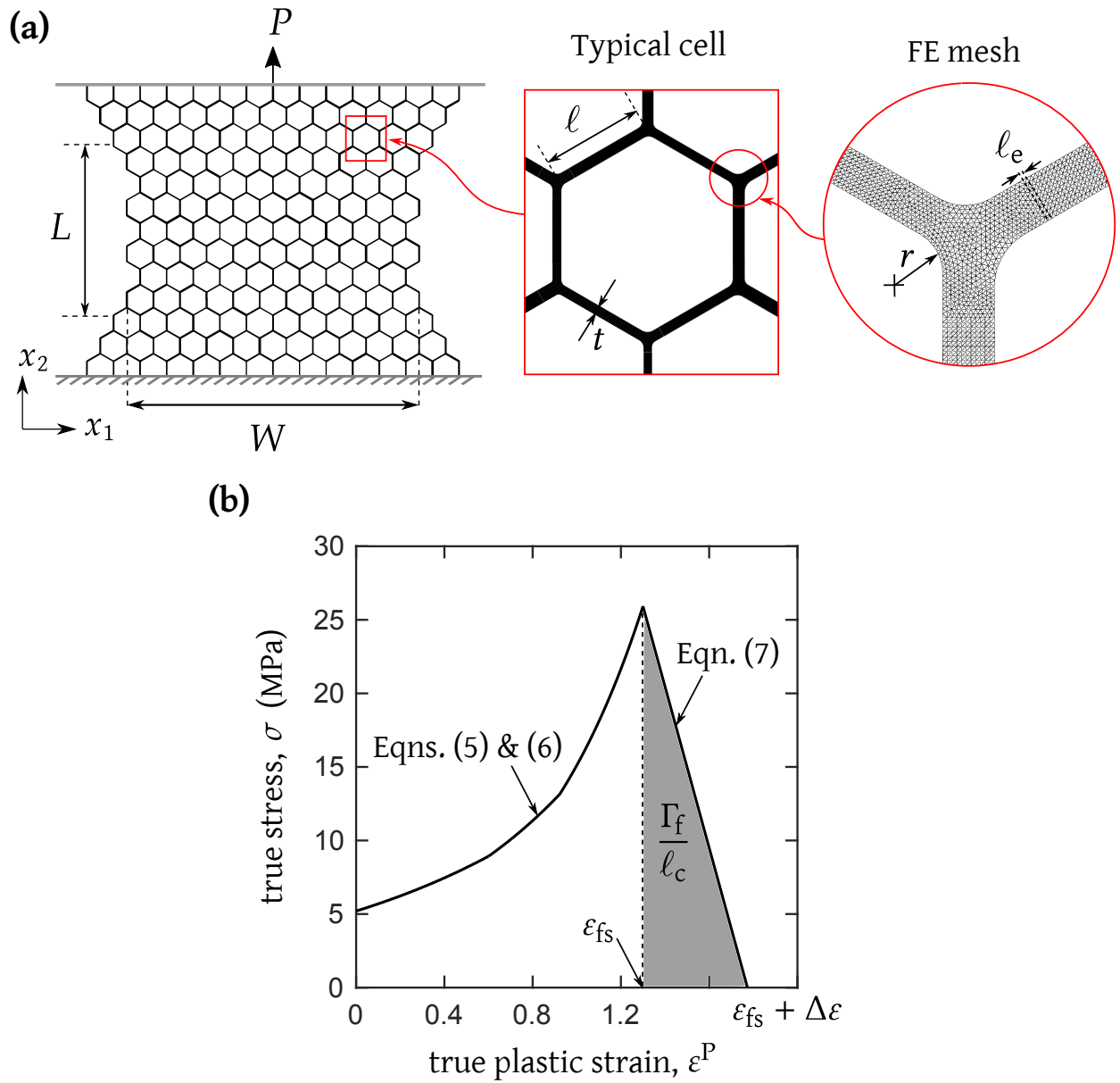


Figure 6: Details of the FE model: (a) geometry of an as-manufactured lattice specimen along with the loading and boundary conditions employed in the FE simulations. A typical cell within the lattice is shown along with the FE mesh at a joint. (b) Assumed true stress versus true plastic strain response of the cell wall solid for $\dot{\epsilon} = 4 \times 10^{-4} \text{ s}^{-1}$.

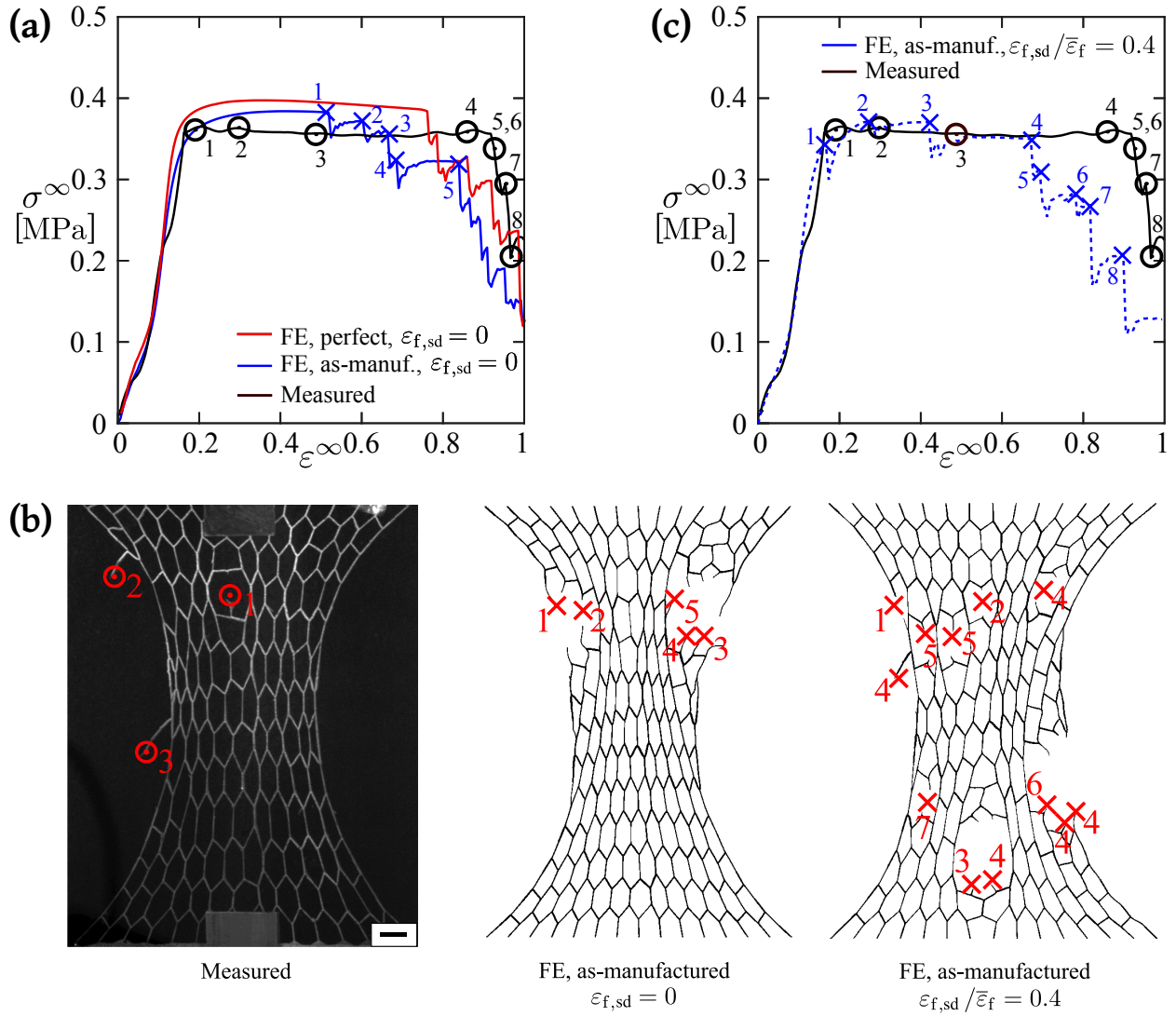


Figure 7: Measured versus predicted response for a lattice of relative density $\bar{\rho} = 0.11$: (a) macroscopic nominal stress σ^∞ versus macroscopic nominal strain of perfect lattices (FE) and one realisation of the as-manufactured lattice (FE and measured); (b) damage state at $\epsilon^\infty = 0.8$. Circles denote the location of strut failure in experiments while crosses denote the predicted failure sites. The numbers in each case denote the position of the strut in the failure sequence. The scale bar is of length 10 mm. (c) Predicted σ^∞ versus ϵ^∞ response in the presence of a dispersion in strut ductility. Measured response for this specimen is included for comparison.

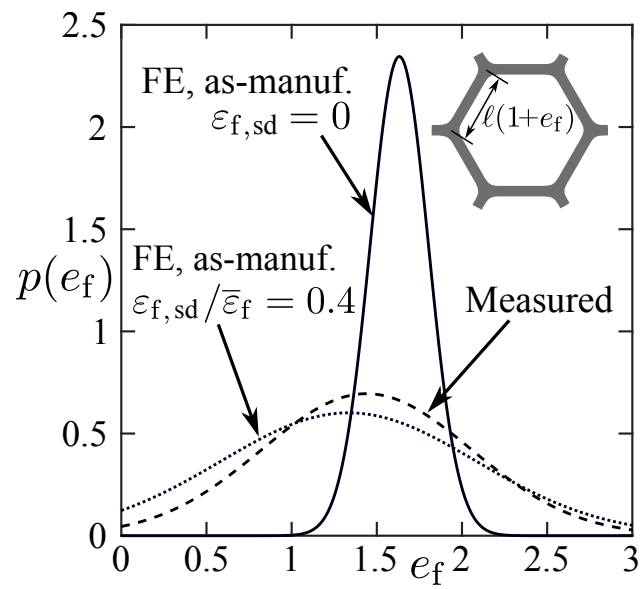


Figure 8: The probability distribution function $p(e_f)$ of the nominal axial failure strain of struts e_f for a lattice of relative density $\bar{\rho} = 0.11$.

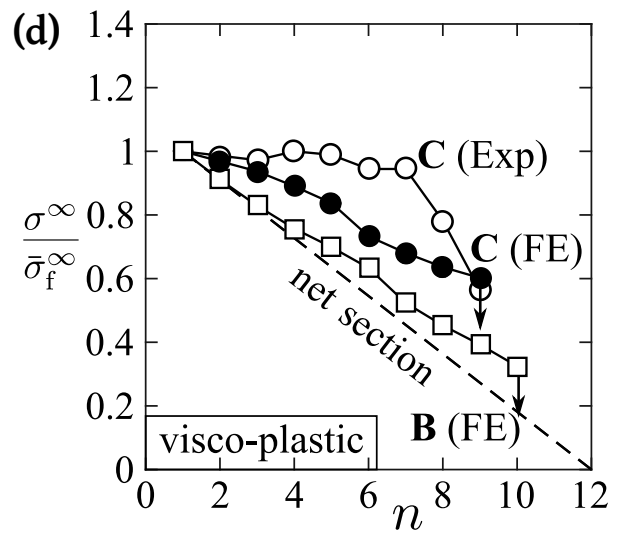
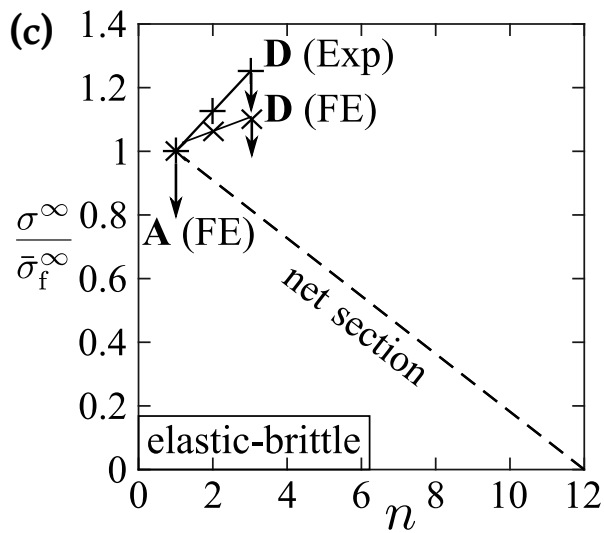
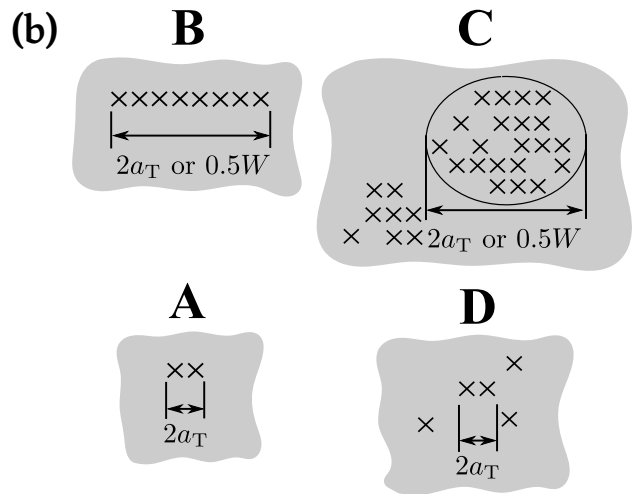
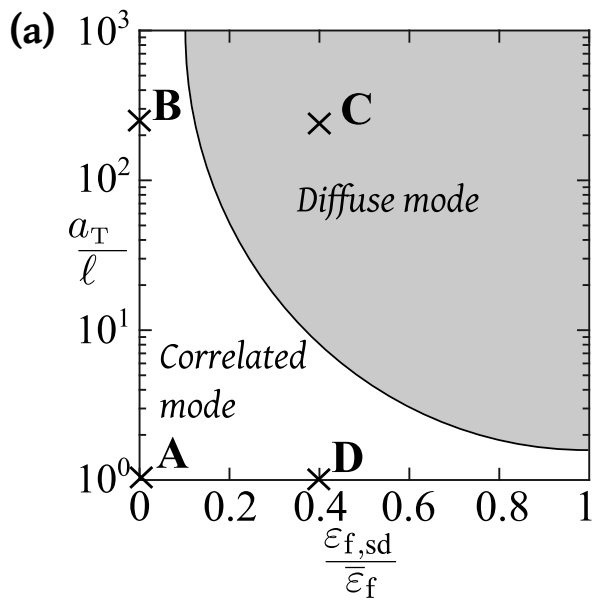


Figure 9: Correlated versus diffuse damage: (a) Map showing the parameter space for correlated versus diffuse modes of damage as a function of transition flaw size a_T/ℓ and the dispersion in strut ductility $\varepsilon_{f,sd}/\bar{\varepsilon}_f$; (b) damage state at onset of fast fracture for cases A through D as labelled in (a). The predicted and measured macroscopic stress during the progressive failure of struts for (c) cases A and D and (d) for cases B and C. These results are for a lattice of $\bar{\rho} = 0.11$.

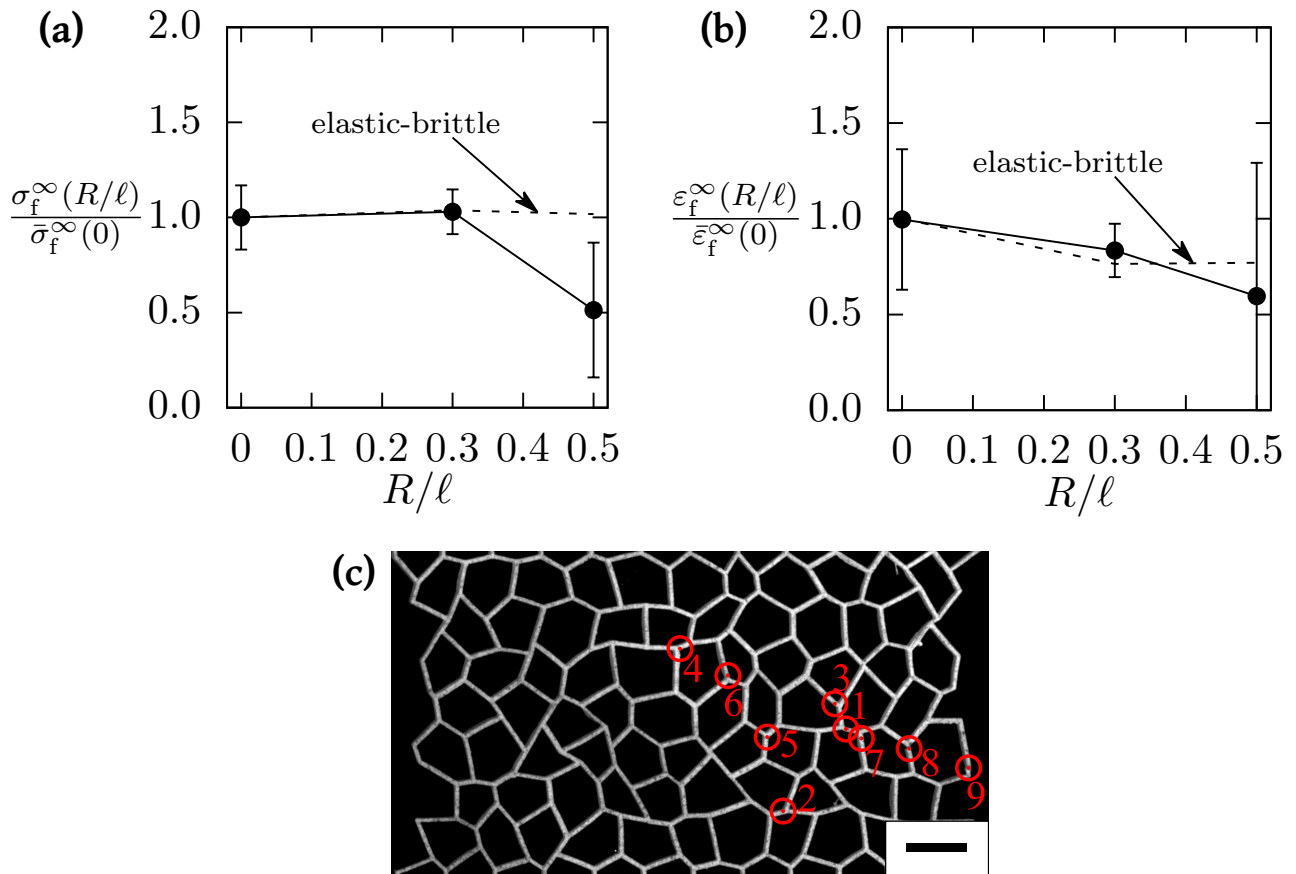


Figure 10: Measured macroscopic properties of imperfect lattices with randomly misplaced joints: (a) macroscopic tensile strength σ_f^∞ and (b) macroscopic tensile ductility ε_f^∞ for first strut failure. The corresponding measured responses for elastic-brittle PMMA lattices as taken from Seiler et al. [13] are included for comparison. (c) Sequence of strut failure in one specimen of $(R/\ell = 0.5)$. The scale bar is of length 10 mm.

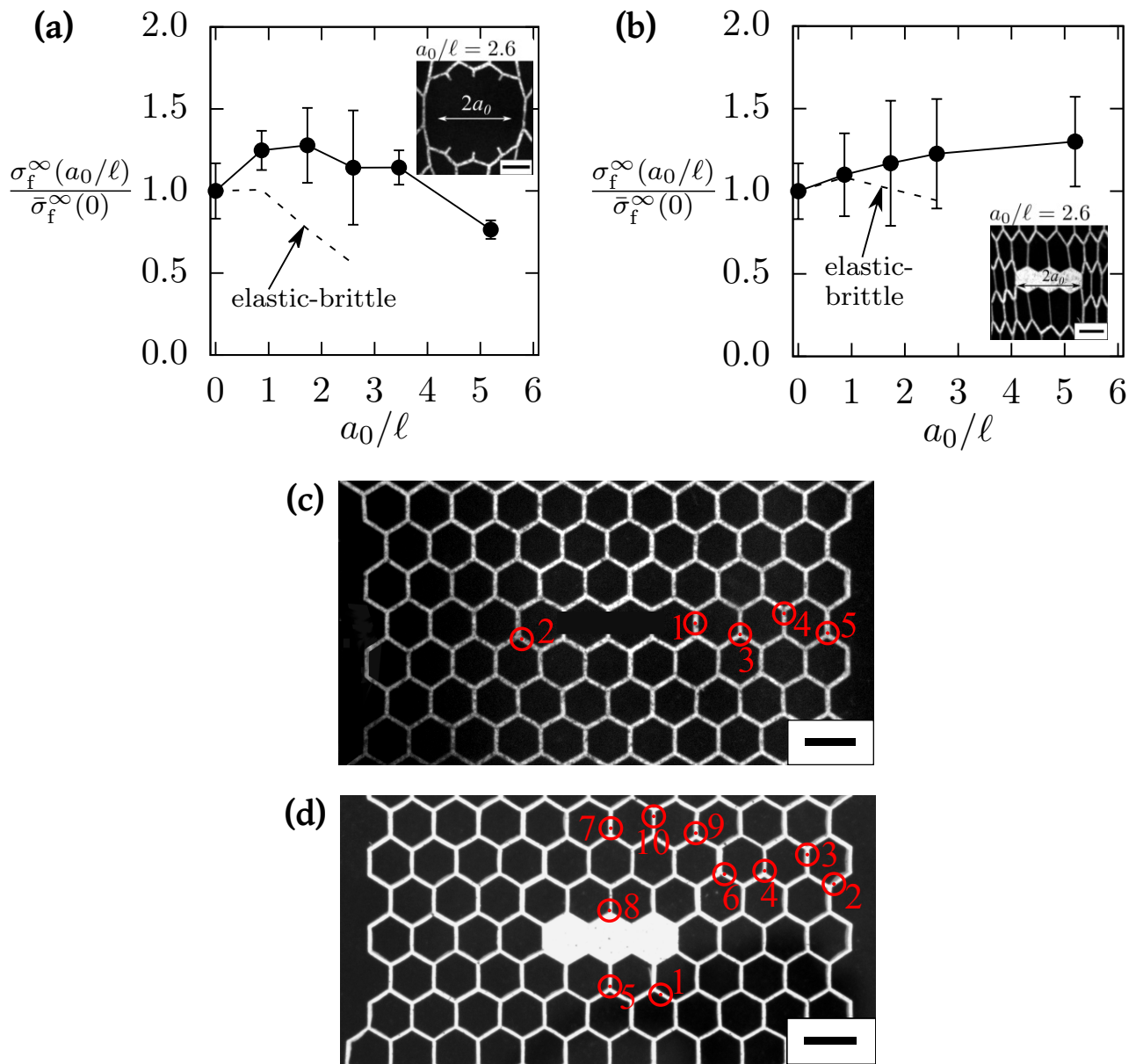


Figure 11: Measured tensile strength of lattice specimens with (a) a row of missing cell walls and (b) a row of solid inclusions, as a function of the defect size a_0/ℓ . The corresponding measured responses for elastic-brittle PMMA lattices as taken from Seiler et al. [13] are included for comparison. A magnified view of the deformed lattice just prior to first strut failure is shown in the insets. Sequence of strut failure in one specimen containing (c) missing cell walls ($a_0/\ell = 2.6$) or (d) solid inclusion ($a_0/\ell = 2.6$). The scale bars are of length 10 mm.